



# Numerical studies of the energy absorption capacities and deformation mechanisms of 2D cellular topologies

Mateusz Majdak<sup>1</sup> · Paweł Baranowski<sup>1</sup> · Jerzy Małachowski<sup>1</sup>

Received: 20 November 2023 / Revised: 29 February 2024 / Accepted: 17 March 2024  
© The Author(s) 2024

## Abstract

This paper investigates the energy absorption capacities of selected cellular topologies under quasi-static loading conditions. Twenty topologies with nearly identical relative densities belonging to 4 groups were examined: honeycomb, re-entrant, bioinspired and chiral. The topologies were modeled using an experimentally validated numerical ABSplus model and subsequently subjected to in-plane uniaxial compression tests. The findings revealed the topologies with the most favorable energy absorption parameters and the main deformation mechanisms. The topologies were classified by mechanism, and a parametric study of basic material properties, namely modulus of elasticity, yield stress, and ductility, was performed for a representative topology from each mechanism. The results indicated that the honeycomb group topologies were characterized by the largest average absorbed energy, and yield stress was found to have the greatest impact on energy absorption efficiency regardless of the main deformation mechanism.

**Keywords** Cellular structures · Additive manufacturing · Auxetic · Energy absorption

## 1 Introduction

Like other metamaterials, cellular structures have tailorable properties. The mechanical properties of cellular structures include high stiffness and strength per unit mass; thus, these materials are commonly used in military, civil, and engineering applications. Since cellular structures undergo controlled deformation, they have great potential in energy absorption applications. For example, they can be adopted in sandwich panels for ballistic protection [1] as inserts in car body components [2], airless tires [3], or motorcycle helmets [4]. Their potential for application was also exploited in aerospace industry [5].

Cellular structures generally consist of thin walls that are connected at their edges to generate three- or two-dimensional (3D or 2D) topologies. 3D topologies are typically associated with lattice structures [6–8] or foam structures [9, 10], whereas 2D topologies are created by dragging

(extruding) cells in the normal direction. Honeycomb (HB) is the most widely studied 2D cellular topology. One of the first works dedicated to this topology was by Gibson and Ashby in 1980 [11]. They developed analytical models of the honeycomb structure based on beam theory and provided analytical descriptions of the elastic moduli and plateau stress of hexagonal honeycomb structures. Researchers have since developed several dozen 2D topologies and analyzed their properties, particularly their energy absorption (EA) capacities [7–11]. These 2D topologies can generally be classified into four groups: honeycomb (HB\_G), re-entrant (RE\_G), bioinspired (BIO\_G), and chiral (CH\_G).

The HB\_G includes several modifications of the original topology, such as adding vertical struts in the middle of cells [12, 13]. Li et al. [12] tested conventional HB, reinforced and kirigami HB topologies in three axial directions under various loading rates. Both modifications, involving the addition of vertical struts in the middle of cells, indicate better crashworthiness properties than traditional honeycomb (KHC, RHC and traditional HB reached 10.02, 10.21 and 8.91 J/g, respectively). Tiwari et al. [13] conducted both experimental tests and numerical simulations to investigate the axial compression behavior of HB and reinforced HB. The influence of relative density on the crushing response of HB was explored by introducing a reinforcement sheet. The addition

✉ Jerzy Małachowski  
jerzy.malachowski@wat.edu.pl

<sup>1</sup> Institute of Mechanics and Computational Engineering,  
Faculty of Mechanical Engineering, Military University  
of Technology, Gen. S. Kaliskiego 2 Street, 00-908 Warsaw,  
Poland

of reinforcement increased relative density, resulting in a significant improvement in crushing strength (25.1 kN for modified honeycomb compared to 19.2 kN for traditional honeycomb). Zhao et al. [14] elucidated the out-of-plane compression behaviors and plastic deformation mechanisms of hierarchical structures through a combination of experimental investigations and analytical predictions. Kagome topology (KHB) demonstrated a smaller relative density and greater densification strains, which contributed to further improvement in EA capabilities. A gradually modified wall thickness proposed by Wu et al. [15] has also been implemented to improve EA of the topologies and they demonstrated that the bi-graded honeycomb could obtain 45.6% higher EA than regular HB (bi-graded absorbed 13.62 kJ/kg compared to 9.39 kJ/kg for regular honeycomb).

The RE\_G is based on the re-entrant hexagonal honeycomb (RE), which possesses the NPR properties. This phenomenon provides special properties, such as high flexural strength, resistance to indentation, and excellent EA capacities. Qi et al. [1] tested a re-entrant-cored sandwich panel as a component of the protective system for concrete structures against close-in blast loads. The auxetic core absorbed 19% more energy than the conventional honeycomb core (8.72 kJ compared to 7.32 kJ). Dhari et al. [16] tested the RE structure under a inclined compression test and several modifications of the RE were proposed and investigated. Ingrole et al. [17] combined RE with HB for the improved SEA by up to 30% (1.013 J/m<sup>3</sup> for auxetic-strut compared to 0.586 J/m<sup>3</sup> for re-entrant auxetic). Varying the thickness of the cell wall in the out-of-plane direction improved the EA efficiency under quasi-static and low-velocity impact loads.

Recent attention has been directed towards structures within the bioinspired group (BIO\_G) and their potential applications in EA [18–20]. Wu et al. [18] identified the crashworthiness characteristic of a bioinspired sandwich structure composed of carbon fiber reinforced plastic (CFRP) panels and aluminum alloy. The crashworthiness characteristics were found to be more sensitive to the length of the core than to the height of the core. Ha et al. [19] introduced a new tubular corrugated configuration inspired by the profile of a coconut tree, named Conical corrugation tube (CGT), which exhibited promising characteristics in terms of EA, initial peak force reduction, and stability during the crushing process. Yang et al. [20] introduced novel bioinspired double-sine corrugated (DSC) sandwich structure to enhance impact resistance. DSC demonstrated significant improvements in structural crashworthiness and a substantial reduction in the initial peak force for regular triangular (1436 N) and for sinusoidal corrugated core (249 N) sandwich panels. Tan et al. [21] proposed a functionally graded lattice structure (FGLS) inspired by a bone architecture. A martensitic TiNi biomaterial was

processed by additive manufacturing (AM), exhibiting higher strength and ductility compared to a uniform lattice with equivalent structural porosity. Post-process heat treatments were employed to alter the microstructure, result in a multi-scale hierarchically strengthened behavior. Li et al. [22] introduced four variants of novel topologies inspired by the lotus root: triangular, quadrangular, and pentagonal. The axial compression properties of these bioinspired sandwich structures (BPSs) were investigated, revealing uniform structural stiffness and excellent EA properties (TBPS exhibited the highest SEA equal 32 kJ/kg). The impact of geometric parameters and cell arrangements on the compression performance of BPS was explored. Zhang et al. [23] indicated that hierarchical structures absorbed up to 2.5 times more energy than traditional HB structures (0.8 J/g for Pomelo peel inspired vs 0.3 J/g for traditional HB).

The chiral topology group (CH\_G) consists of topologies with rigid circular nodes connected to each other by tangential ligaments. Depending on the number of ligaments connected to the node, chiral structures are classified as tetrachiral (four connections), hexachiral (six connections), or trichiral (three connections). For tetrachiral and trichiral structures, anti-tetrachiral and anti-trichiral structures can be obtained when ribs are connected to the same side of the node. Elastic constants for chiral topologies under in-plane loading have been derived by Alderson et al. [24]. Hierarchical modification of anti-tetrachiral structures for generating enhanced and tunable mechanical properties has been proposed by Wu et al. [25]. Hu et al. [26] established the influence of the characteristic dimensions of the elementary cell ratio on EA. The in-plane crushing response of the tetrachiral design has been studied experimentally and numerically under static and dynamic loads.

Novel topologies are usually compared with the hexagonal honeycomb and two or three other topologies. However, a direct comparison of topologies from several groups is necessary to assess the influence of geometric features on energy absorption (EA) and deformation characteristics. Therefore, the present paper compared selected topologies from the four groups discussed above. The comparison included five previously studied topologies in each group except for the re-entrant group, which included three established topologies and two topologies proposed by the authors. The simulations focused on uniaxial quasi-static compression tests and were followed by a validation of the numerical methodology and constitutive parameters of the ABSplus material. The primary objectives of this paper were to analyze the relationships between material parameters and geometry shape of a unit cell, select the most efficient topologies for future parametric studies and improve the EA performance of these topologies. Furthermore, basic material properties such as modulus of elasticity ( $E$ ), yield

stress ( $R_c$ ), and effective plastic strain at failure ( $EPFS$ ) were comprehensively evaluated, and the parameters with the greatest influence on EA were identified and related to the main deformation mechanism of the selected topology.

As mentioned in the previous section, the main objective of this paper was to analyze the EA properties and the deformation behavior of selected cellular topologies with different geometric features. Twenty topologies in four groups, namely HB\_G, RE\_G, BIO\_G, and CH\_G, were tested. The five topologies in each group are listed in Table 1 and briefly described as follows.

### 1.1 HB\_G topologies

The topologies in the HB\_G included original HB, triangle honeycomb (THB), honeycomb with horizontal added struts (HBAS), and KHB. The well-known HB is a starting point for many studies of cellular geometries [27–29]. Baranowski et al. [27] designed and manufactured using Ti–6Al–4V alloy powder. The honeycomb structures were subjected to a quasi-static compression test. An elastoviscoplastic material model was employed to predict the material behavior. Agreement between the histories of deformation, failure, and

forces indicates the effectiveness of the numerical model in capturing the behavior of the material. Konarzewski et al. [28] fabricated two regular cellular structures which were fabricated using fused deposition modeling (FDM) with ABSplus material. Structures were examined under various deformation velocities and categorized as quasi-static and dynamic. It allowed us to understand the deformation behavior of the structures under various loading conditions. Kucewicz et al. [29] introduced a novel approach to modeling the failure of a honeycomb structure manufactured using 3D-printing technology, particularly FDM with ABSplus material. Two alternative methods using constitutive models were considered. Liu et al. [30] investigated the impact of cell micro-topology on in-plane dynamic honeycomb crushing through explicit dynamic FE simulation. They studied HB topologies with equilateral triangular and quadratic cell and regular and staggered arrangements. Han et al. [31] proposed the triangular gradient thinning (GTT) HB structure. The efficiency of modulus, strength, and EA was evaluated. Hamzehei et al. [32] investigated 2D octagonal auxetic meta-material using numerical and experimental approaches. An octagonal structure showed NPR at high compressive strain and a parametric study was carried out to obtain the best

**Table 1** Characteristics of the cellular topologies analyzed in the study

Group	Topology	Primary properties	Source
HB_G	HB	Excellent EA properties, long plateau	Baranowski et al. [27]
	OHB	Better buckling resistance than traditional HB, good stability and periodicity, stable deformation mechanism, NPR	Hamzehei et al. [32] Hedayati et al. [33]
	HBAS	Better EA compared to traditional HB both in-plane and out-of-plane, long plateau	Tiwari et al Thomas et al
	KHB	High equivalent stress under in-plane loading, excellent crashworthy behaviors, balanced in-plane and out-of-plane properties	Qiu et al. [36] Zhang et al. [35]
	THB	Higher in-plane strength than bending-dominated structures	Han et al. [31]
RE_G	RE	Excellent impact resistance, resistance, NPR	Kalubadanage et al. [37]
	SHRE	Two plateau stages during compression, great EA, stable deformation	Wei et al. [42]
	BRE	Sharp angles replaced by hexagonal HB, two plateau stages, great EA potential	An et al. [43]
	OG1	Stable deformation with a plateau stage, great EA potential	Authorship
	OG2	Stable deformation with plateau stage, global deformation during compression process	Authorship
BIO_G	BSW	Controlled EA possibilities, better EA capacities than traditional HB	He et al. [51]
	BGS	Structural hierarchy, 2.63 times higher plateau stress than the traditional HB	Fang et al. [44]
	BHS	Using sinusoidal struts effectively enhances EA compared to traditional HB	An et al. [43]
	BOS	Superior mechanism for withstanding loads, extraordinary out-of-plane EA performance, plateau stage	Fernandes et al. [46]
	BBS	Excellent EA performance under axial load, structural hierarchy	Hu et al. [49]
CH_G	TCH	Sensitive to strain rate rather than geometric dimensions, NPR, EA potential	Qi et al. [55]
	ACH	NPR in both lateral directions, different deformation mechanisms under compression along different directions	Hu et al. [26]
	HCH	NPR, better EA under low velocities, dissipates plastic strain energy in two stages: ligament buckling and node buckling	Gao et al. [53]
	REATCH	NPR even under large deformation, four stages of deformation	Hu et al. [54]
	ATCH	Highest EA among tested HB and RE, NPR	Johnston et al. [56]

auxetic properties. Hedayati et al. [33] explored the mechanical properties of a novel octagonal geometry, manufactured using FDM with polylactic acid (PLA). Compression tests were conducted, and mechanical properties, including elastic modulus, yield stress, and Poisson's ratio, were determined. The octagonal honeycomb exhibited yield stress and elastic modulus values comparable to regular HB. The HBAS was selected because comprehensive studies have shown that this geometry improves crash performance properties [34, 35]. Thomas et al. [34] focused on the in-plane compression analysis of reinforced aluminum honeycomb. Both numerical and experimental approaches were employed. The KHB was selected because an investigation of this geometry carried out by Zhang et al. [35] under compression in two planes showed that it improved plateau stress and EA compared to HB [35]. The deformation behavior of KHB has been compared with periodic triangular, square, rhombus, and hexagonal planar lattices, which was presented in the study by Qiu et al. [36].

## 1.2 RE\_G topologies

This study examined three previously reported re-entrant topologies: the classic RE, the star-triangular geometry (SHRE), and the bidirectional re-entrant honeycomb (BRH). The other two topologies, OG1 and OG2, are original to this paper. RE modifies HB by creating an obtuse angle between the vertical struts, resulting in auxetic deformation. RE was the first example of an auxetic topology and can be manufactured using traditional manufacturing methods, such as the corrugated sheets presented in Kalubadange [37], allowing full-scale blast tests. The crashworthiness properties of RE have been studied extensively [38–40]. For instance, Günaydin et al. [40] developed a numerical model to simulate the compressive behavior of multi-material RE under quasi-static loading, and experimental validation was performed. Multi-material approach significantly enhanced SEA (2.19 kJ/kg for Nylon + Carbon fiber for Re-entrant compared to 1.26 kJ/kg for pure Nylon), compressive strength (3.03 MPa for Nylon + Carbon fiber compared to 1.14 MPa for pure Nylon for Re-entrant), and modulus values (16.64 MPa for multi-material compared to 12.71 MPa for pure Nylon). Choudry et al. [38] investigated the in-plane EA characteristics of RE and modified RE produced through fused filament fabrication, incorporating parametric analysis and geometry optimization. Geometrical parameters, such as the strut-length ration and joint angles, were examined for their influence and interaction effects on the stiffness, and EA features. Xiong et al. [39] focused on the quantitative optimization of a modified RE's NPR addressing challenges related to overhanging struts by replacing them with inclined ones. Modification was aimed to eliminate the need for support structures required in the

selective laser melting process. The calculated Poisson's ratios revealed that the optimal simulated inclination angle for the struts is  $9^\circ$ , with a corresponding optimum RE angle of  $79^\circ$  and a strut thickness of 0.9 mm. Wang et al. [41] introduced a novel RE star-shaped, which has attracted attention for its promising mechanical properties, particularly in EA applications. The study identified two plateau stress regions under low-velocity impact, with the second plateau stress approximately twice that of the first. Wei et al. [42] conducted an in-plane compression study of SHRE topology in both directions, and a stable deformation with the pronounced NPR was revealed in the in-plane direction. The NPR effect in the 2-direction was found to be weaker, and numerical simulation models were established to comprehensively understand both small and large deformation behaviors of the structure. An et al. [43] replaced sharp angles with hexagonal shapes to create the BRH, which has excellent SEA (at 3 m/s the BRH absorbed 0.613 kJ/kg compared to 0.522 and 0.374 for SSH and QSH, respectively) under high velocities during crushing. OG1 is similar to a star-shaped honeycomb, but differs in the use of a smaller rhombus to connect the star-shaped cells in the vertical direction. OG2 is a modification of the classic RE in which the sharp edges are replaced by fillets and circular nodes to enable two-stage deformation.

## 1.3 BIO\_G topologies

Through evolution, living organisms have developed numerous multicell structures with high strength, high EA, and low density to survive in specific habitats. Some of these structures can be observed with the naked eye, but the majority are visible only with proper magnification. In this article, topologies inspired by grass stems (BGS), spiderwebs (BSW), bamboo stems (BBS), the ocean sponge *Euplectella aspergillum* (BOS), and horseshoes (BHS) were selected. BGS is a second-order hierarchical honeycomb studied by Fang et al. [44]. Quasi-static tests were conducted experimentally to analyze the crushing behaviors, followed by corresponding FEA. It was found that its plateau stress is up to 2.6 times greater than that of HB and 4.6 times greater than that of aluminum foam with the same relative density. Chen et al. [45] analytically investigated BGS the in-plane parameters under compression. The results revealed that increasing the hierarchical level increases the SEA. BHS is a modification of the classic HB to improve its EA parameters, which was proposed by An et al. [43]. Numerical results have confirmed that adding a horseshoe mesostructure enhances the mechanical properties of the topology. The promising properties of BOS have been confirmed by quasi-static in-plane and out-of-plane compression tests [46–48]. Fernandes et al. [46] through a combination of finite-element simulations and mechanical test on 3D-printed specimens

with various lattice geometries. Using an evolutionary optimization algorithm, the research demonstrated that the sponge-inspired lattice geometry approaches the optimal material distribution within the considered design space. Wang et al. [47] involving finite-element simulations and experimental tests, demonstrate superior compression behaviors and energy absorption capacity under out-of-plane direction. The proposed topology exhibited microfolding lobes with shorter wavelengths, leading to enhanced energy absorption and higher efficiency in energy absorption. Li et al. [48] indicated that the proposed topology has a higher SEA than conventional structures. Finally, BBS was previously tested under axial crushing force rather than in-plane compression [49, 50]. Hu et al. [49] studied BBS through dynamic drop-weight impact experiments and demonstrated high SEA (even 38.6 J/g); further parametric

simulations explored the influence of different parameters on the characteristics of EA [50]. He et al. [51] examined the out-of-plane crashworthiness of spider-web hierarchy honeycomb. The energy absorption capability increases significantly with properly adjusted hierarchical parameters. The results revealed that for the first-order spider-web hierarchy honeycomb, specific energy absorption increased by 62% compared to the hexagonal honeycomb.

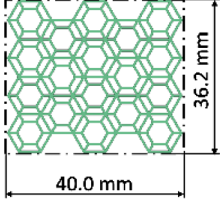
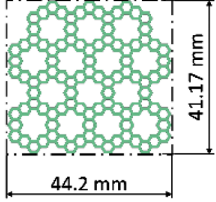
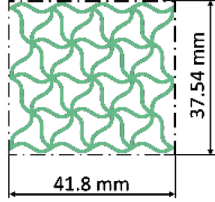
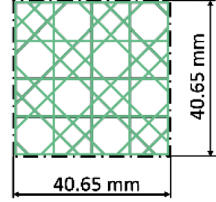
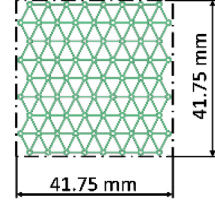
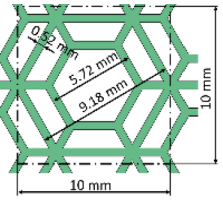
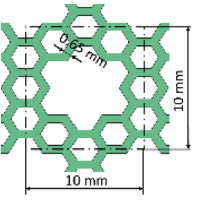
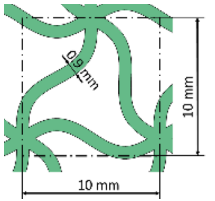
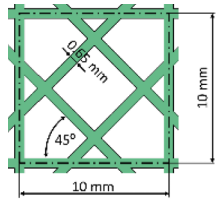
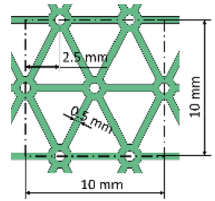
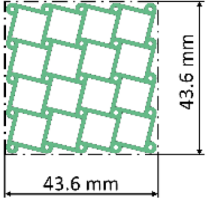
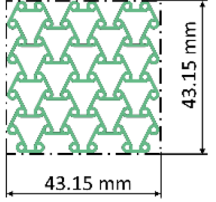
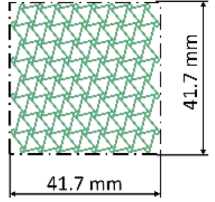
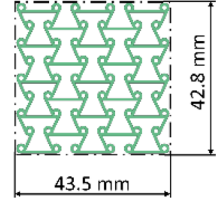
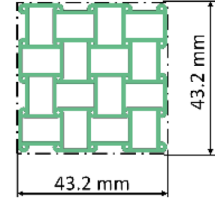
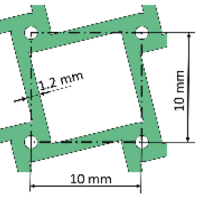
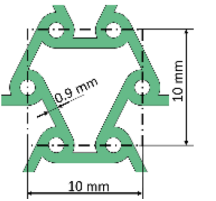
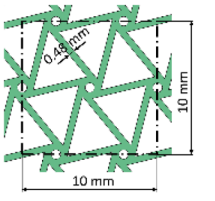
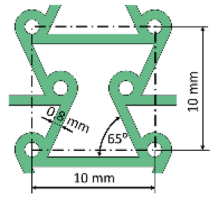
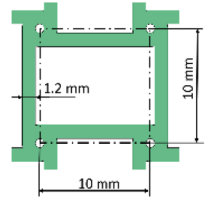
### 1.4 CH\_G topologies

The following chiral topologies were tested in this paper: tetrachiral (TCH), anti-chiral (ACH), hexachiral (HCH), re-entrant anti-tetrachiral (REATCH) and anti-tetrachiral (ATCH). Hu et al. [26] established theoretical analytical models to predict both the NPR and the crushing stress

**Table 2** Geometric properties of all topologies

HB_G				
HB	OHB	HBAS	KHB	THB
RE_G				
RE	SHRE	BR	OG1	OG2

Table 2 (continued)

BIO_G				
BSW	BGS	BHS	BOS	BBS
				
40.0 mm	44.2 mm	41.8 mm	40.65 mm	41.75 mm
36.2 mm	41.17 mm	37.54 mm	40.65 mm	41.75 mm
				
10 mm	10 mm	10 mm	10 mm	10 mm
10 mm	10 mm	10 mm	10 mm	10 mm
0.82 mm	0.62 mm	0.62 mm	0.65 mm	2.5 mm
5.72 mm	5.72 mm	5.72 mm	45°	0.6 mm
9.38 mm	9.38 mm	9.38 mm		
CH_G				
TCH	ACH	HCH	REATCH	ATCH
				
43.6 mm	43.15 mm	41.7 mm	43.5 mm	43.2 mm
43.6 mm	43.15 mm	41.7 mm	42.8 mm	43.2 mm
				
10 mm	10 mm	10 mm	10 mm	10 mm
10 mm	10 mm	10 mm	10 mm	10 mm
1.2 mm	0.9 mm	0.48 mm	0.8 mm	1.2 mm
			65°	

of ACH. The study provided insight into the design considerations for these topologies, considering parameters such as ligament length ratio and wall thickness. Lorato et al. [52] focused on the out-of-plane linear elastic mechanical properties of trichiral, TCH, and HCH. Combining analytical, numerical, and experimental approaches, this study provided a comprehensive understanding of the out-of-plane linear elastic mechanical properties of chiral HBs. The results of the uniaxial compression testing of HCH under dynamic conditions presented by Gao et al. [53] indicated that the chiral structure had greater plastic energy dissipation capacity than the other topologies tested when subjected to relatively low impact velocities and a crushing strain of 70%. The numerical and analytical studies of REATCH presented by Hu et al. [54] revealed stable deformation curves with a distinct plateau region. Four stages of the deformation curve were observed, and experimental tests validated the accuracy

of both testing methods. On the other hand, Qi et al. [55] performed quasi-static experimental tests and prediction of the crushing strength using theoretical models and numerical simulations and showed that the optimized arrangement of a unit cell in TCH improved shock resistance. Johnston et al. [56] investigated the effect of using multiple material within three cellular geometries: anti-tetrachiral, re-entrant, and hexagonal honeycomb. Three different combinations of materials were used: pure PLA, PLA-nylon combination, and PLA-TPU. In all cases, the highest energy absorption values were reached by anti-tetrachiral.

## 2 Methodology for numerical modeling and simulations

### 2.1 Geometric properties of the models

To allow an effective comparison of the results, all topologies had similar geometric properties: a relative density of 0.3. This required varying wall thicknesses for each topology: unit cell dimension of 10.0 mm × 10.0 mm and four cells in the vertical and horizontal directions. Due to the specific arrangement of cells in HB, HBAS, and KHB, more cells were used in these topologies. Each geometry is presented with its characteristic dimensions in Table 2.

### 2.2 Model description and assumptions for finite-element (FE) studies

A numerical approach was used to investigate the four groups of topologies under quasi-static uniaxial compression. Each model was developed based on the methodology and considerations presented in previous papers [27]. All numerical computations were performed using an explicit multi-parametric processing (MPP) LS-Dyna solver [57] to easily consider material failure and numerical erosion during FEA. A 1.0-mm section of model thickness with the appropriate symmetry conditions applied to the outer faces has previously been shown to provide a credible model for simulating compression tests [27]. This approach not only reduces computational time but also fully reproduces the deformation process of the cellular structure in an effective manner. A mesh sensitivity study was not conducted because the mesh parameters were previously analyzed [27]. For each model, three hexahedral elements were assumed through the wall thickness, resulting in an average element size of approximately 0.3 mm. The cell specimen was inserted

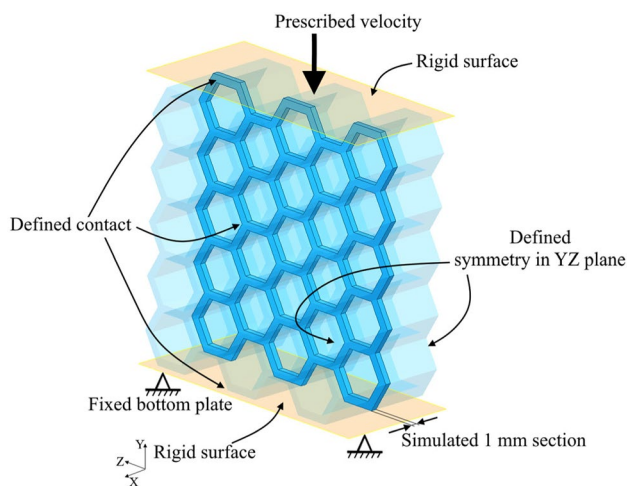


**Fig. 1** Scheme of the numerical model with initial and boundary conditions

between two rigid walls to simulate the compression test; one of the surfaces was fixed, while the second was able to move according to the prescribed velocity described using an equation for which inertia was significantly minimized [27]:

$$v(t) = \frac{\pi}{\pi - 2} \frac{S_{\max}}{T} \left[ 1 - \cos\left(\frac{\pi}{2T}t\right) \right] \tag{1}$$

where  $T$  is the termination time of the simulation and  $S_{\max}$  is the final displacement of the rigid surface.

The representative numerical model with appropriate initial boundary conditions is presented in Fig. 1.

The interaction between the parts was reproduced by adopting a penalty-based contact procedure with the friction coefficients determined in previous studies [27]. Ultimately, a friction coefficient of  $\mu=0.2$  for the interior contact in the topology and for the rigid wall-topology contact interaction was used for all simulated cases.

An elastoviscoplastic constitutive model was used to reproduce the compressive behavior of the ABSplus material. This model is extremely effective for simulating the deformation process of cellular structures in uniaxial compression tests. This model is based on the Huber–Mises–Hencky (HMH) yield criterion in which deviatoric stresses  $S_{ij}$  satisfy the yield function  $\sigma_y$  as follows [57]:

$$\phi = \frac{1}{2} S_{ij} S_{ij} - \frac{\sigma_y^2}{3} \leq 0, \tag{2}$$

$$\sigma_y = \beta \left[ \sigma_0 + f_h(\epsilon_{eff}^p) \right] \tag{3}$$

where  $\epsilon_{eff}^p$  is an effective plastic strain defined as

$$\epsilon_{eff}^p = \int_0^t d\epsilon_{eff}^p \tag{4}$$

where  $\beta$  is a strain rate effect parameter (omitted in the present studies), and  $f_h$  is the hardening function, which can be specified in tabular form. However,  $f_h$  is usually defined as a linear function [57]:

$$f_h(\epsilon_{eff}^p) = E_p(\epsilon_{eff}^p) \tag{5}$$

where  $E_p$  is the plastic hardening modulus.

The evolution of damage is represented by  $\omega$ , which varies from 0 to 1 (no damage and complete rupture) and can be defined according to the increase in  $\epsilon_{eff}^p$  as follows [57]:

$$\omega = \frac{\epsilon_{eff}^p - \epsilon_{failure}^p}{\epsilon_{rupture}^p - \epsilon_{failure}^p}, \quad \epsilon_{failure}^p \leq \epsilon_{eff}^p \leq \epsilon_{rupture}^p \tag{6}$$

**Table 3** Mechanical properties of ABSplus used in the MPD model [28, 29]

Constant	ABSplus	Unit
Density, $\rho$	1040.0	kg/m <sup>3</sup>
Elastic modulus, $E$	2200.0	MPa
Poisson's ratio, $\nu$	0.35	–
Yield Stress, $R_e$	30.0	MPa
EPFS	8.71	%

**Table 4** Points of the damage curves of ABSplus used in the MPD model [28, 29]

Point no	ABSplus	
	Eff. plastic strain [%]	Damage [–]
1	0.00	0.0
2	8.71	0.8
3	100	0.8
4	200	1.0

**Table 5** Points of the ES-EPS curve of ABSplus used in the MPD model [28, 29]

Point no	ABSplus	
	Eff. plastic strain [%]	Effective stress [MPa]
1	0.00	30.00
2	0.08	30.45
3	0.17	30.71
4	0.25	30.89
5	0.54	31.08
6	1.20	31.27
7	3.10	31.44
8	8.71	31.72

According to (6), once the effective plastic failure strain (EPFS)  $\epsilon_{failure}^p$  is exceeded, softening begins until the rupture strain  $\epsilon_{rupture}^p$  is reached (the FE are removed from the model when the erosion criterion is satisfied).

Tables 3, 4 and 5 present the basic mechanical properties, stress vs. strain points at the plastic region and damage points of ABSplus used in the material plasticity with damaged (MPD) model, respectively. The parameters were taken from previous studies [28, 29].

### 2.3 Simulation strategy

The numerical model was adopted to carry out several simulations according to the following stages. First, a

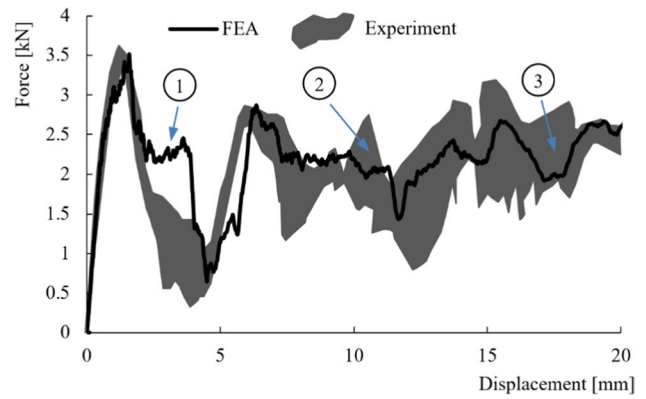


**Fig. 2** Comparison of force versus displacement curves from experimental tests and FEA (the shaded area represents the limiting curves from the experimental tests)

validation analysis of the model for a quasi-static uniaxial compression test of HB was performed. Next, numerical simulations of the 20 topologies described in Tables 1 and 2 were carried out, and the topologies were compared based on the force vs. displacement curves, SEA, and deformation mechanisms. The most efficient representatives of each group in terms of EA were identified. Finally, the influence of basic material properties was studied for three topologies with different main deformation mechanisms (determined in the previous stage): plastic joint, global deformation, and bending ligaments. The influence of  $E$ ,  $R_e$ , and EPFS was analyzed for the three deformation mechanisms.

## 3 Results and discussion

### 3.1 Model validation

Uniaxial quasi-static compression tests were performed using an ElectroForce 3300 universal strength machine at a room temperature of 23 °C. Five specimens were used, and each topology was compressed up to 50% shortening of the specimen. Details of the experimental procedures and numerical methodologies can be found in previous articles [27]; only the results are discussed below. A Dimension 1200es SST (Stratasys Corp.) 3D printer was used to manufacture the described structures using the fused deposition modeling technique with ABSplus material. Failure behavior and force versus displacement curves were compared to assess the credibility of the model. The validation process was based on an HB cell geometry with dimensions of 40.0 × 40.0 × 20.0 mm (width × height × depth). In previous works [27–29], a slightly different relative density was used compared to the present numerical simulations (35% vs. 30%); however, it was assumed that the results would demonstrate a sufficient



level in confidence of the proposed model. Identical conditions and numerical model parameters were used in all numerical simulations in this paper.

In Fig. 2, the force characteristics obtained from finite element analysis (FEA) are compared with the experimental results measured for five specimens. Laboratory results are represented by a shaded zone corresponding to the area between the limiting curves. The numerical curve generally followed the experimental force characteristics, with similar numbers of drops and rises. The initial slopes were nearly identical, and the first peak value differed from the experimental measurement by less than 2.0%. After the initial peak, the curve shapes obtained by FEA differed due to the implementation of the damage curve to maintain the material continuity longer. However, these differences

were slight, and very good reproduction of the force versus displacement curve was obtained, with an average force of 1.82 kN, 11.7% lower than the experimental value of 2.06 kN. The corresponding EA value (37.7 J) was also in close agreement with the experimental results (36.9 J).

The topology deformation confirmed the very good reproduction of the force characteristic, as shown in Fig. 3, which compares selected stages of the compression process with corresponding screenshots from the camera. Excellent reproduction of the behavior of the specimen was observed: the failure began in the shear plane and passed through the fourth cell at the height of the HB and the specimen corner in the vicinity of the rigid wall. The subsequent collapse of the cell layers was observed both numerically (FEA) and experimentally.

**Fig. 3** Comparison of the honeycomb deformation process in the experimental tests and FEA at selected stages of compression

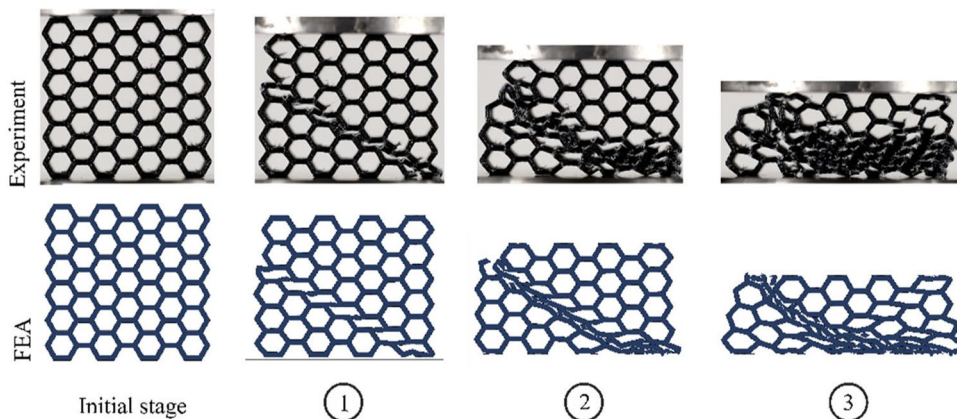
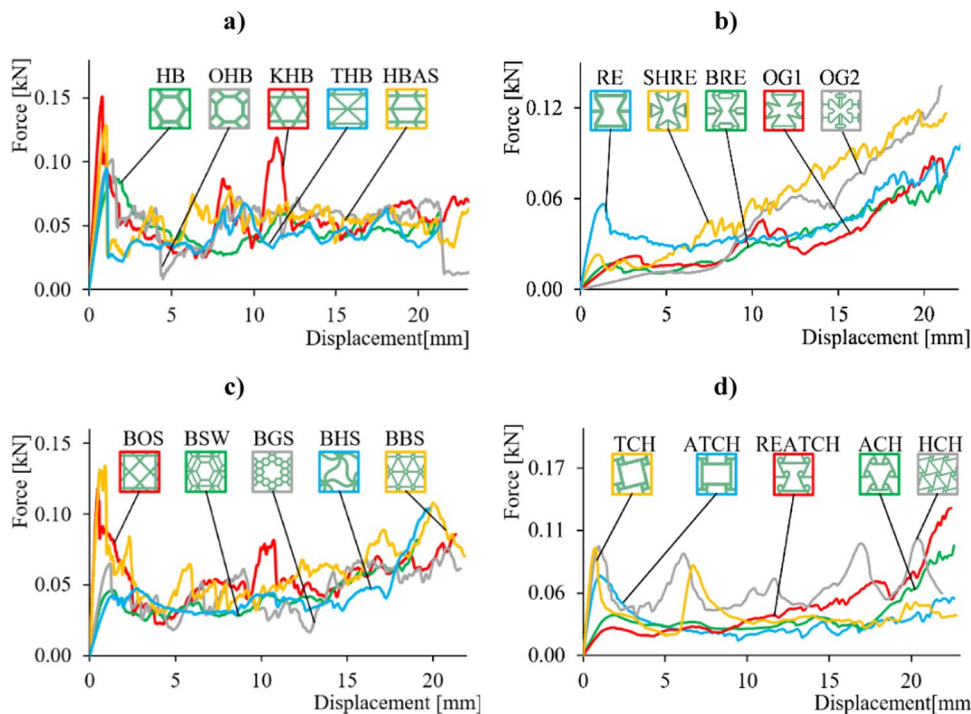


**Fig. 4** Force versus displacement curves of the **a** HB\_G, **b** RE\_G, **c** BIO\_G and **d** CH\_G



### 3.2 Force versus displacement curves

The validated model was used to perform numerical simulations of all 20 topologies; the resulting force vs. displacement curves are presented in Fig. 4. Even though the same material parameters were used, the slopes of the pre-peak curves differed, indicating that the stiffness varied depending on the topology. The shapes of the force characteristics of the topologies differed depending on the failure mechanism and the deformation process. However, for the three groups (Fig. 4a: HB\_G, Fig. 4c: BIO\_G and Fig. 4d: CH\_G), a similar trend was observed with the peak force at the beginning and fluctuations in the other parts of the curves. On the contrary, the topologies in the fourth group (RE\_G—Fig. 4b) had a large force increase after ~12.0 mm of displacement, which is mainly caused by the earlier densification of the structures in this group compared to the other three (see Figs. 6, 7, 8, 9).

Figure 4a presents HB\_G. The peak force was highest for KHB (150 N) and lowest for HB (85 N). KHB and HBAS had the highest stiffness values. The overall behavior was similar for all topologies and included increases and drops in force, an instant loss of stiffness after reaching the maximum force, and subsequent distinctive fluctuations caused by further deformation. However, for OHB and HB, the force decreased gradually rather than rapidly, and plateau-like characteristics of post-peak deformation were observed for HB and HBAS.

Figure 4b presents the force vs. displacement curves of RE\_G. Plateau regions were observed for BRE, OG1, OG2 and RE. The stiffness differed significantly and was highest and lowest for RE and OG2, respectively. Only RE exhibited an initial peak force; after reaching its maximum value (57.0 N), the curve dropped to a medium level. A plateau was observed in the RE curve up to a displacement of 16.0 mm, which was caused by cell densification. Stable deformation of the OG1 and OG2 topologies was observed up to 15–17 mm of compression. SHRE had the most oscillatory curve, with no apparent plateau.

The force versus displacement curves of BIO\_G are presented in Fig. 4c. BBS and BOS were the stiffest topologies. Compared to the other topologies, BBS reached a much higher peak force of 132.0 N. The force curves decreased rapidly after the initial peak, and this decrease was followed by visible drops and increases. BGS exhibited two main peaks with similar values. BSW and BHS had the lowest peak force values, but both exhibited stable deformation behavior without notable fluctuations; a plateau was visible for almost the entire duration of compression. Strength increased only toward the end as a result of densification of the structure.

Figure 4d shows the force histories of the CH\_G. Differences between topologies were more pronounced in

this group than in the other three groups. The topologies differed not only in stiffness but also in the course of the curves and the number of peaks throughout the compression process. TCH and HCH had similar elastic regions, and their maximum force values at the initial peak were close to 90 N. Although these topologies had the highest force peak values in the group, the force characteristics included numerous rises and drops, which were worst for TCH. ATCH, ACH, and REATCH exhibited more stable deformation during compression, and the latter two did not exhibit initial peak forces.

### 3.3 Energy absorption capacities

For all topologies, the SEA parameters were calculated. To evaluate the energy absorption capacity of all structures, and its expression is

$$SEA = \frac{\int_0^u F(u)du}{m}$$

where  $m$  is the mass of structures, and  $F(u)$  and  $u$  are the force and displacement of upper plate during compression up to 50% of structures' height, respectively.

Figure 5 compares the SEA (EA normalized to mass) values of the 20 topologies. The topologies were classified into three categories by SEA. The first category consisted of ATCH to REATCH and had  $SEA < 1.5$  J/g. ATCH had the lowest SEA, 1.09 J/g, which is more than 50% smaller than the highest SEA. This category included four of the CH\_G topologies, indicating that this topology group had poorer EA capacities. The second category comprised BSW to OG2 and had SEA values of 1.58–1.78 J/g. Notably, three of the seven topologies in this category were BIO\_G. The third category had the best SEA and included BOS to SHRE. BBS from BIO\_G and SHRE from RE\_G had the highest SEA; both topologies absorbed nearly 2.5 J/g. The other five topologies in the third category (HCH, OHB, KHB, HBAS

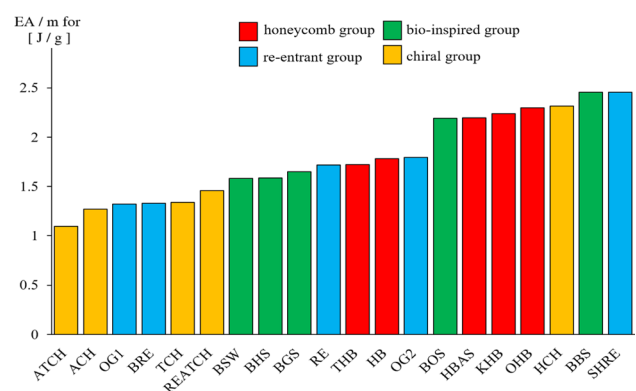


Fig. 5 Comparison of the SEA of the 20 topologies

**Table 6** SEA of the four groups of topologies and the main deformation mechanisms

Group	Topology	SEA [J/g]	Average SEA [J/g]	Main deformation mechanism
HB_G	HB	1.78	2.10	} Plastic joint/shear
	OHB	2.30		
	HBAS	2.2		
	KHB	2.24		
	THB	1.72		
RE_G	RE	1.72	1.72	} Global deformation
	SHRE	2.46		
	BRE	1.33		
	OG1	1.32		
	OG2	1.79		
BIO_G	BSW	1.58	1.89	} Plastic joint/shear
	BGS	1.65		
	BBS	2.46		
	BOS	2.19		
	BHS	1.59		Bending ligaments
CH_G	TCH	1.34	1.50	} Bending ligaments
	ACH	1.27		
	HCH	2.32		
	REATCH	1.46		
	ATCH	1.10		

and BOS) had SEA values ranging from 2.19 J/g for BOS to 2.32 J/g for HCH. Three of the topologies in the third category were from HB\_G.

To further compare the topology groups and determine which deformation mechanism provides better EA performance, the average SEA was calculated. The deformation mechanisms in each group are presented in Sect. 4.4. The results are presented in Table 6, which also provides the SEA and average SEA values. HB\_G had the largest average SEA, 2.15 J/g, followed by BIO\_G (1.89 J/g), RE\_G (1.72 J/g) and CH\_G (1.49 J/g). The calculated SEA values for the three main deformation mechanisms are presented in Table 7.

### 3.4 Deformation comparison

In this section, the deformations of the topologies due to compression loading are discussed, and the most efficient topology in each group in terms of EA is identified: OHB, SHRE, BBS and HCH from HB\_G, RE\_G, BIO\_G and CH\_G, respectively. The deformation processes are shown for four successive stages, starting with the undeformed geometry, through 10% and 30% structure deformation, and ending at 50% compression (shortening).

Figure 6 presents the deformation process of the topologies in HB\_G. HB and OHB behaved similarly, and failure began within a geometric diagonal in one shear plane, which was followed by the collapse of neighboring cells until the last stage of the deformation. The failure patterns

**Table 7** Average SEA for each deformation mechanism and associated topologies

Main deformation mechanism	Topology	Average SEA [J/g]
Plastic joint/shear	HB	2.0
	OHB	
	HBAS	
	KHB	
	THB	
	BSW	
	BGS	
	BBS	
Global deformation	BOS	1.72
	RE	
	SHRE	
	BRE	
	OG1	
Bending ligaments	OG2	1.51
	TCH	
	ACH	
	HCH	
	REATCH	
	ATCH	
BHS		

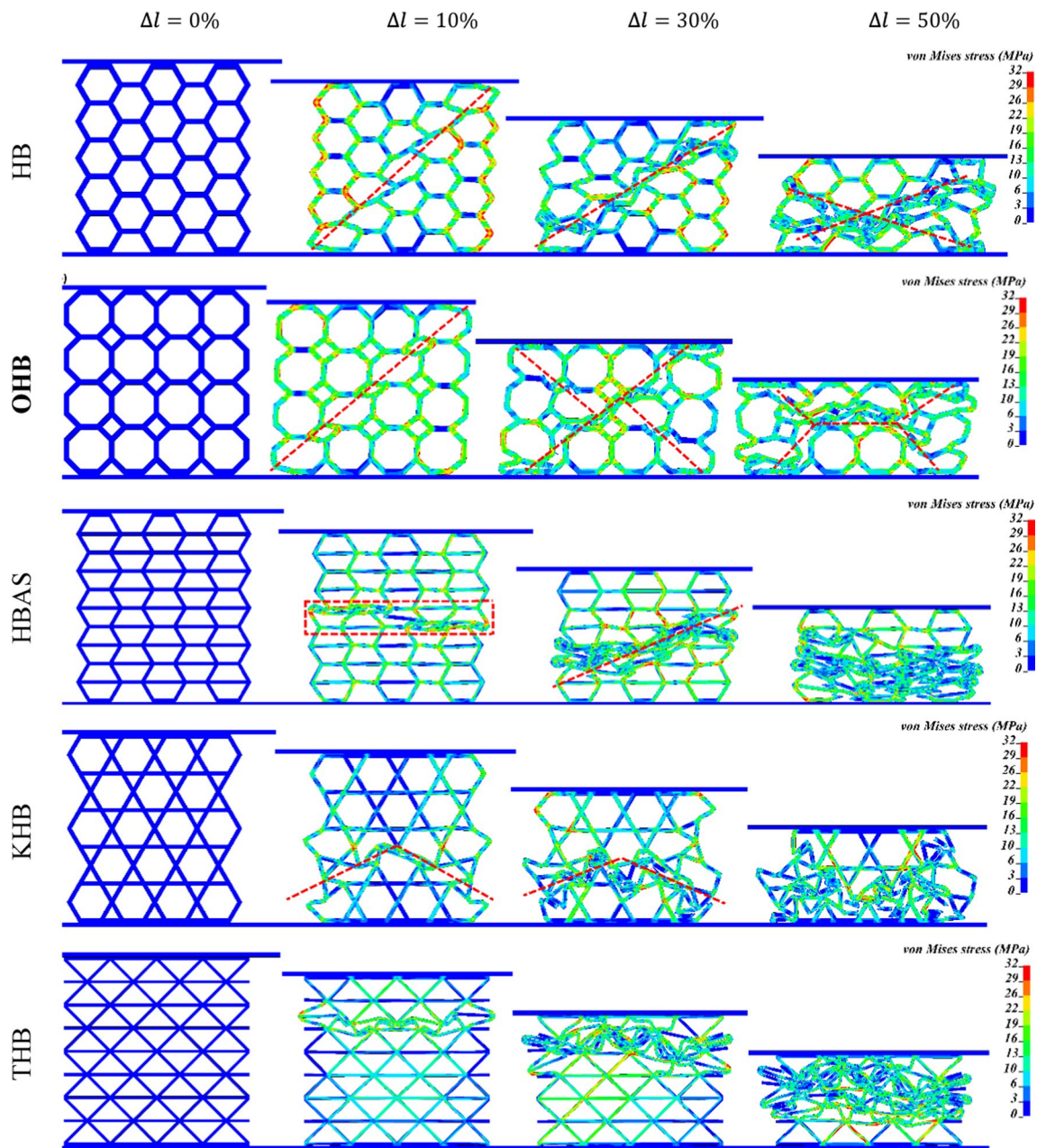


**Fig. 6** Deformation stages of the topologies in HB\_G

of HBAS and THB were significantly different from those of HB and OHB. For HBAS and THB, failure began in the middle or upper layer of cells, respectively, perpendicular to the compression direction. As the compression progressed, successive layer-by-layer collapse occurred. KHB exhibited a V-shaped failure at the middle of its height until reaching total deformation at 50% compression.

The deformation processes of the five topologies in RE\_G differed from those in HB\_G and are presented in Fig. 7. Auxetic deformation was evident for all five topologies. The

vertical struts transferred the load in the initial stages before buckling (SHRE, BRE) or bending (RE, OG1, OG2). Until the vertical struts collapsed, the horizontal struts were not involved in the transfer of the load force. After 30% compression, several cells within the topology closed, and their walls began to interact with neighboring cells until the last stage of the deformation process.

Figure 8 presents the successive stages of deformation of the five topologies in BIO\_G. BOS, BSW, and BBS exhibited similar deformation, with failure beginning on

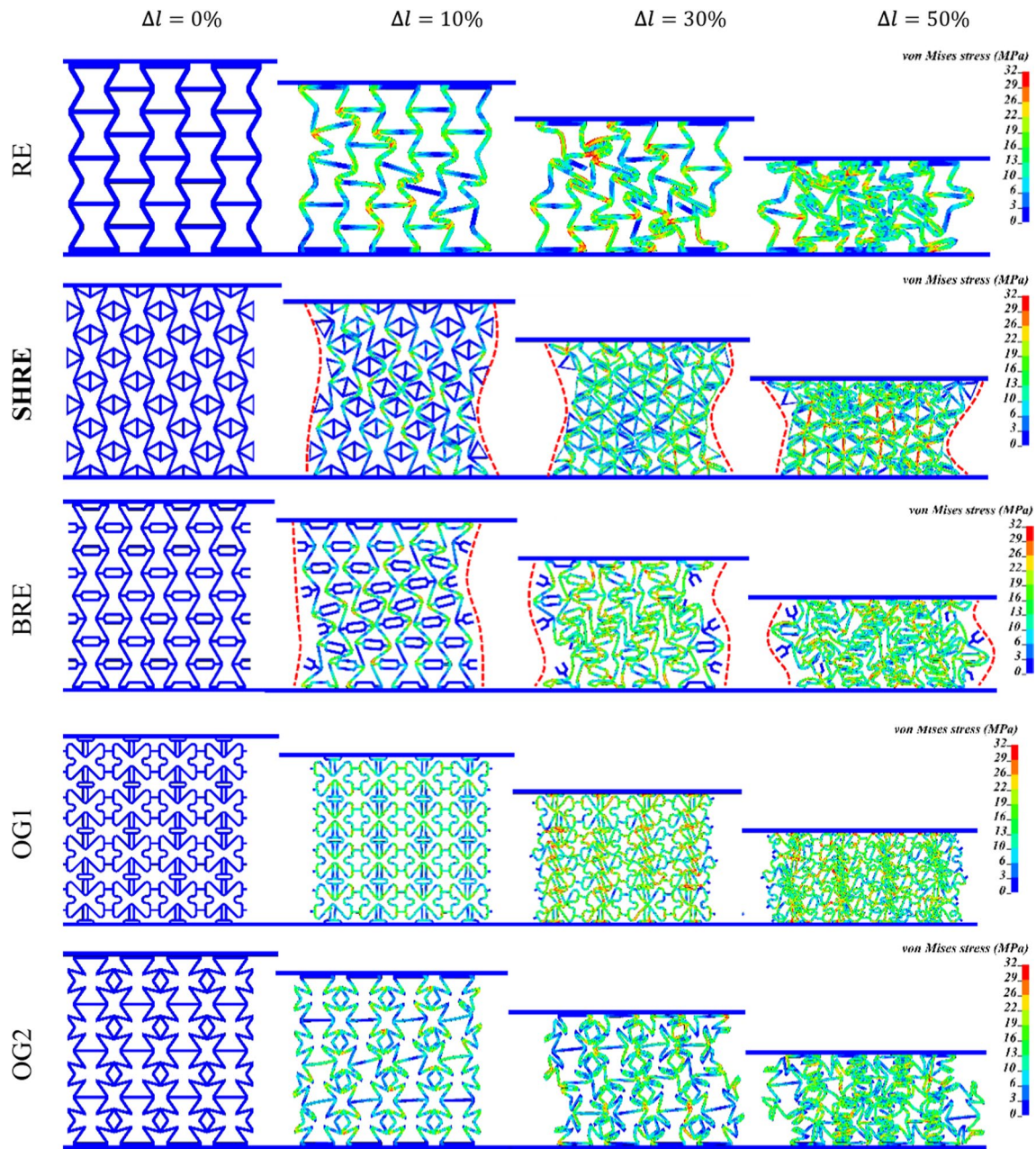


**Fig. 7** Deformation stages of the topologies in RE\_G

the diagonal. Further compression resulted in an X-shaped failure pattern that reached 70% (BSW and BBS) or 50% (BOS) of the initial specimen height. By comparison, the four stages of deformation of BHS revealed different failure characteristics. For BHS, structure failure was caused by loss of stability and subsequent bending of the ligaments in the diagonal plane. Material fracture (reproduced as FE erosion) was observed in the later stages of specimen compression until it reached 50% of its height. For BGS, the initial stages of deformation reveal the presence of shearing bands. As the compression continues, the continuity between the upper

and lower parts of the specimen is lost, leading to a rapid crushing effect.

The deformation stages of CH\_G topologies are presented in Fig. 9. REATCH and ACH behaved similarly: bending of the ligaments of the structure under the applied load resulted in the rotation of the nodes (joints) and a V-shaped deformation mechanism. Furthermore, the load was almost uniformly distributed over the structure. At 50% compression, the entire structure collapsed. The other three topologies in CH\_G had different failure characteristics. In TCH, the struts lost stability and began to bend (at 10% shortening of

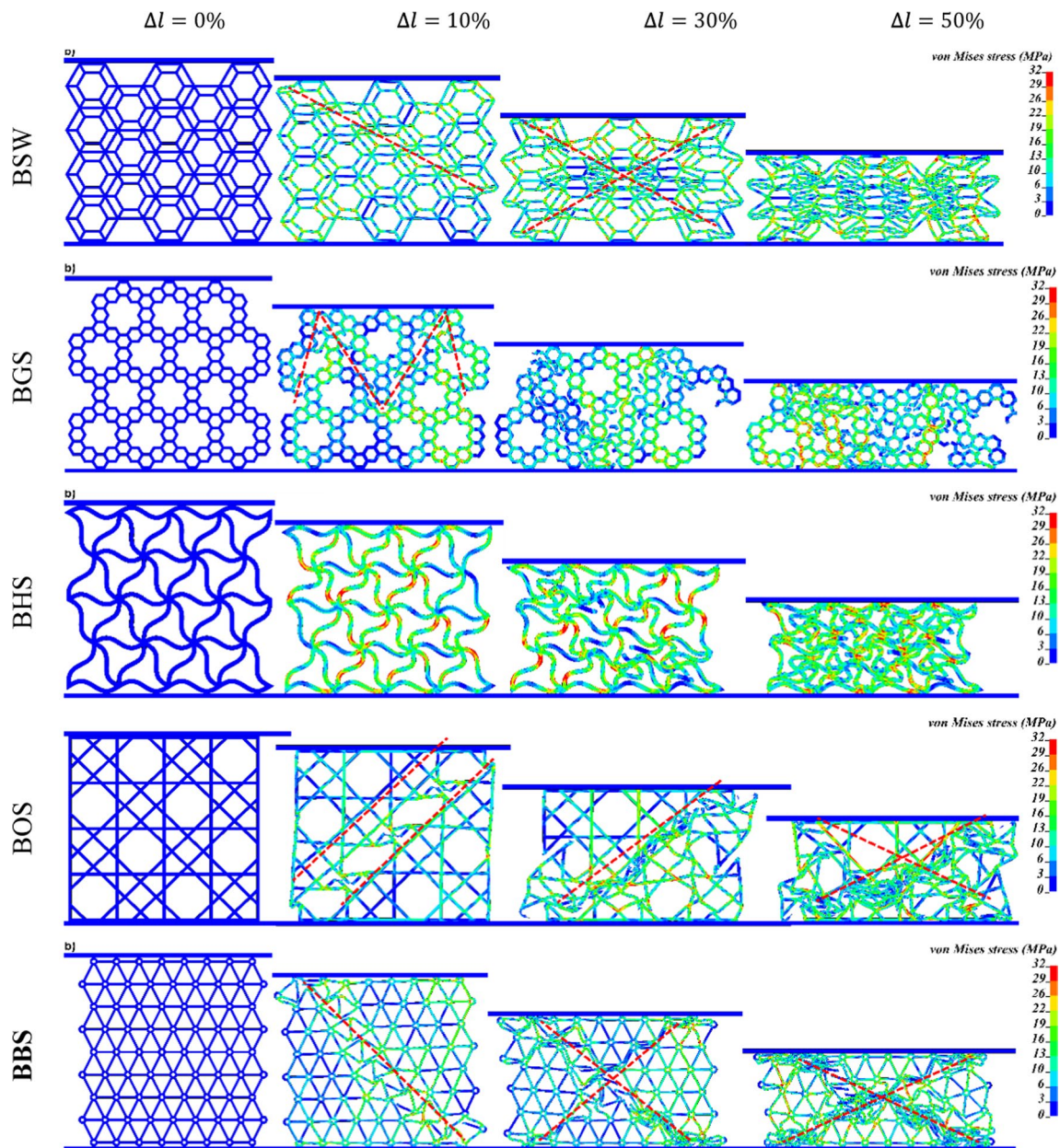


**Fig. 8** Deformation stages of the topologies in BIO\_G

the sample) and rotate. This phenomenon occurred within the bottom and upper layers of the sample. Successive layer-by-layer collapse continued as compression progressed. On the contrary, ATCH exhibited deformation of almost all struts, leading to collapse of the entire structure. Strong bending of the material occurred until full compaction at 50% compression. The HCH began to deform in the middle of its height, and a strongly localized bending of the struts within the strut joints was observed. At 30% of  $\Delta l$ , the direction of the inclination changed, with more layers deformed, and almost all unit cells collapsed, with no distinctive shape.

### 3.5 Analysis of the influence of material properties

In this section, the results of the parametric study of material properties are discussed. Based on the analysis of deformation processes, the topologies were classified according to the main deformation mechanisms: *global, plastic joint/shearing* and *bending ligaments* (see Table 6). In the first category of topologies, most of the struts are involved in the compression process and buckling and/or bending occurs. In the second category of topologies, strong plastification occurs within the cell joints, mainly due to shearing. The third category of topologies mainly undergoes

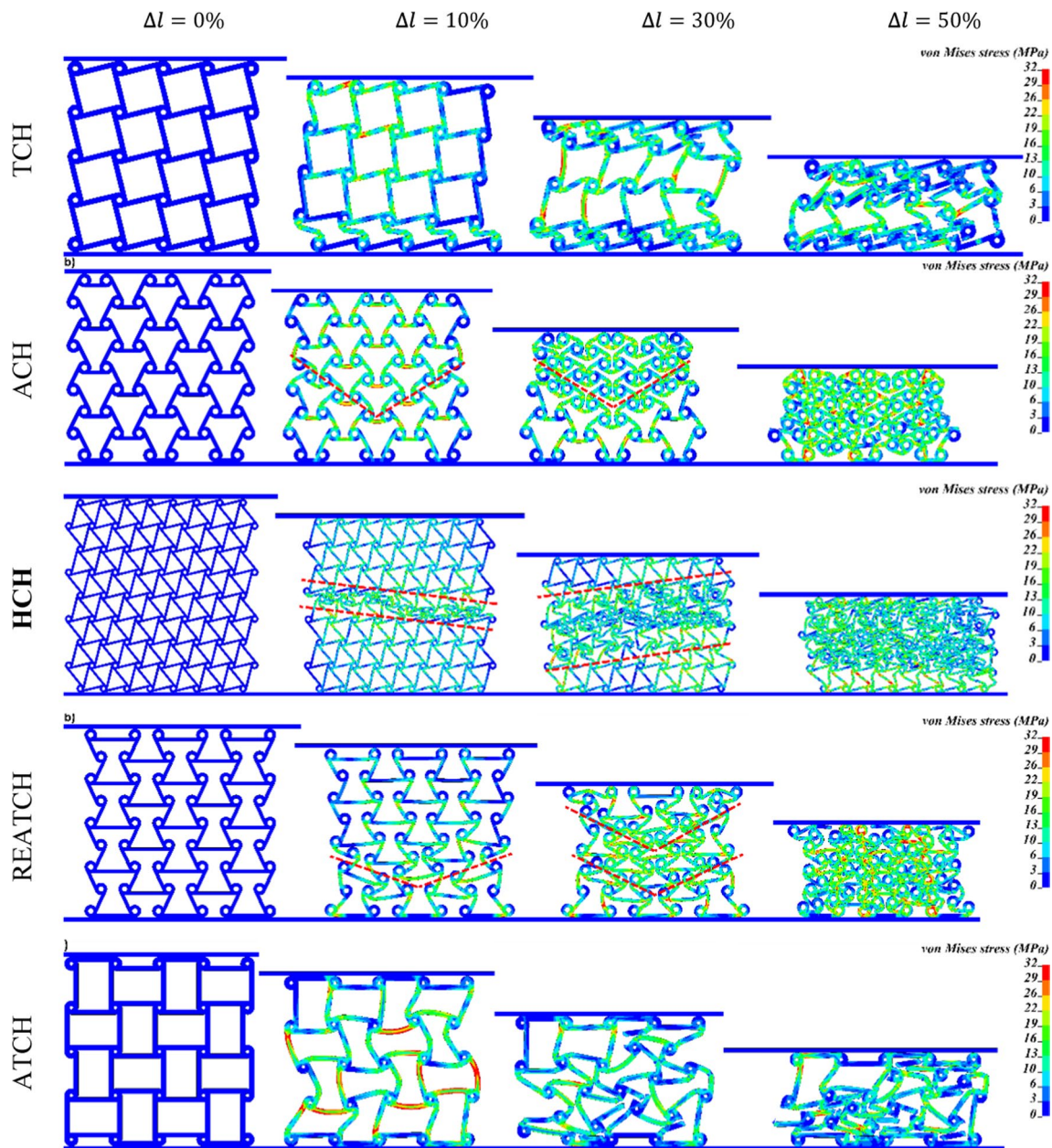


**Fig. 9** Deformation stages of the topologies in CH\_G

bending within the joint, which acts as a rotational hinge until full collapse of the topology. SHRE, BGS, and BHS were selected as perfect representatives of the global, plastic joint/shearing and bending ligaments mechanisms, respectively (Fig. 10). SEA values were compared with respect to three material parameters, namely  $E$ ,  $R_e$ , and  $EFPS$ , to assess the influence of stiffness, maximum strength, and ductility, respectively, on EA capacities.

Different values of these parameters for ABSplus filaments were selected between the minimum and maximum values found in the literature. One parameter was varied, while the other two were set to the original values shown in

Table 3. Table 8 summarizes the simulated cases to provide a better understanding of the methodology.

The results for the influence of  $E$  (Young's modulus) are presented in Fig. 11, which shows the SEA vs.  $E$  curves for the three investigated topologies. In general, SEA increases with increasing  $E$ . The influence of  $E$  on SEA was smallest for BHS, in which the bending of the ligaments plays a crucial role in the deformation process (the struts begin to bend very early due to their specially designed shape; Fig. 8). For SHRE (Fig. 7), in which the vertical struts supported by horizontal ligaments transfer the load, a pronounced effect of  $E$  on SEA was expected but was not observed. BGS, which

**Fig. 10** Graphical representation of the main deformation mechanisms: **a** global (SHRE), **b** plastic joint/shearing (BGS), and **c** bending ligaments (BHS)

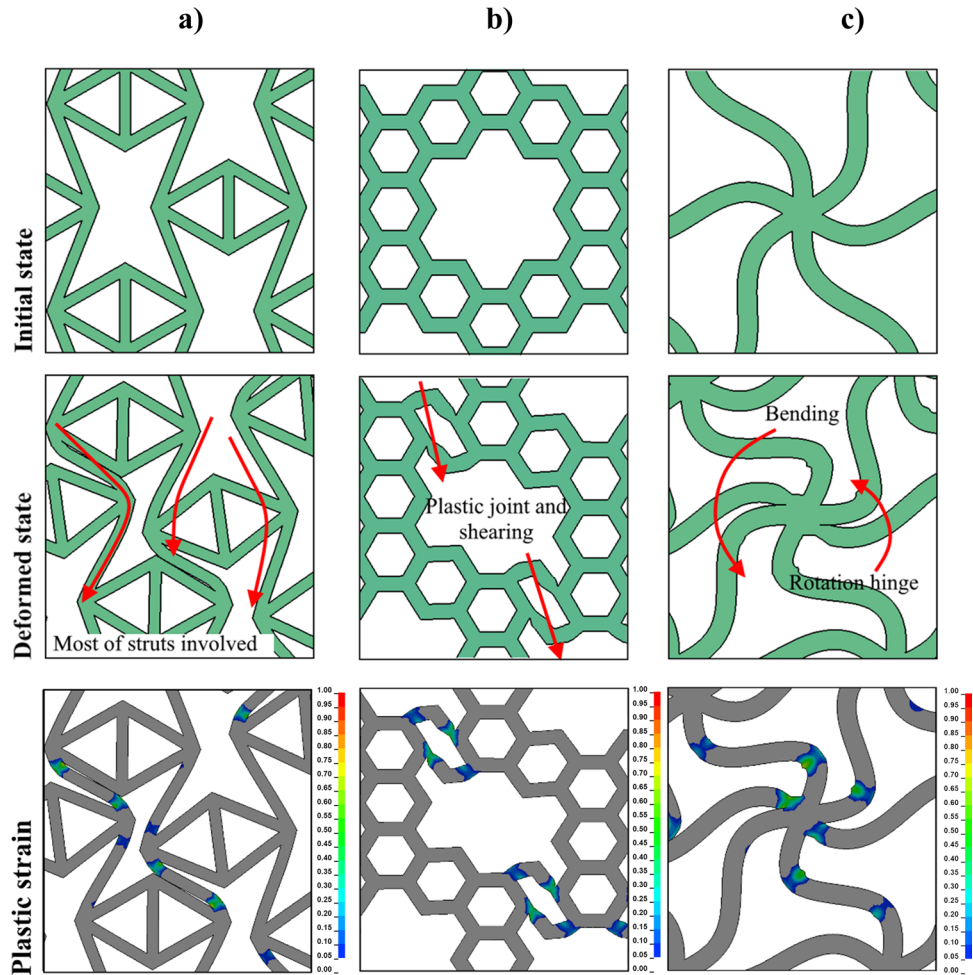


**Table 8** FEA conditions with the three parameters analyzed

Analyzed parameter	Parameter values in each FEA		
	$E$ [MPa]	$R_e$ [MPa]	$EFPS$ [%]
Young's modulus, $E$	1250.0	30.0	8.71
	1500.0		
	1750.0		
	2000.0		
	2200.0		
Yield stress, $R_e$	2200.0	26.0	8.71
		30.0	
		38.0	
		58.0	
		71.0	
Effective plastic strain at failure, $EFPS$	2200.0	30.0	2.71
			8.71
			12.71
			16.71
			20.71

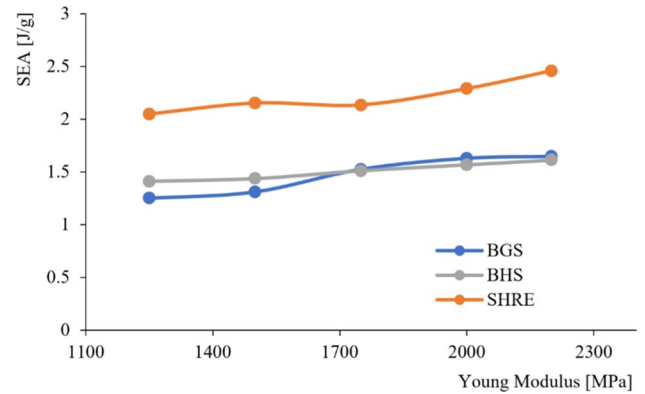


**Fig. 11** Influence of Young's modulus  $E$  on the SEA of the three topologies with different main deformation mechanisms

exhibited the most brittle failure (Fig. 8), exhibited a non-linear curve, indicating that the stiffness of ABSplus had the greatest effect on the EA efficiency of this topology.

The SEA histories of the topologies under different yield stresses are presented in Fig. 12. The influence of  $R_e$  was more pronounced than that of  $E$ . In general,



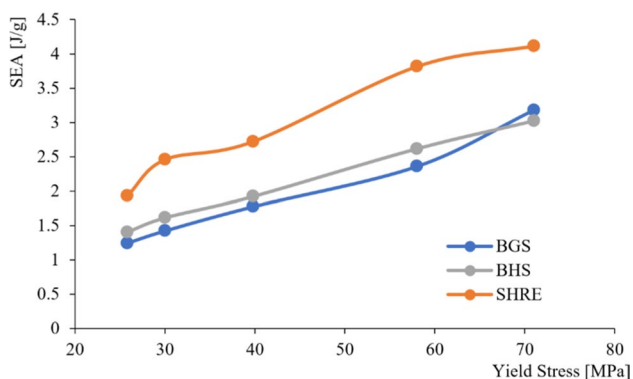


Fig. 12 Influence of the yield stress  $R_e$  on the SEA of three topologies with different main deformation mechanisms

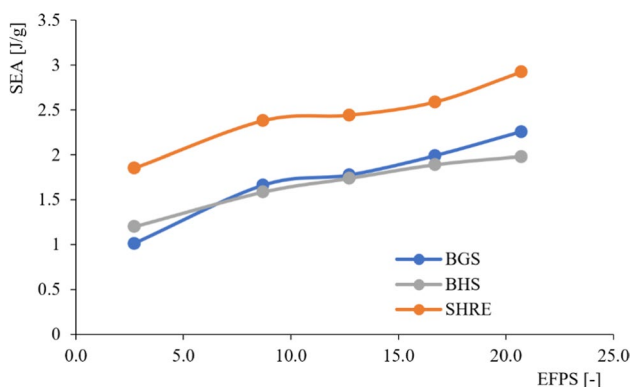


Fig. 13 Influence of the effective plastic failure strain  $EFPS$  on the SEA of the three topologies with different main deformation mechanisms

linear characteristics were obtained for all three topologies, although a nonlinear influence between  $R_e = 26.0$  MPa and  $R_e = 30.0$  MPa was observed for SHRE. In particular, the difference in SEA values between the smallest and highest  $R_e$  values was more than twice as high for SHRE than for the other two topologies.

The influence of  $EFPS$  on the EA capacities of the three topologies is shown in Fig. 13. As expected, this parameter had the most pronounced effect on BGS, which exhibits brittle failure during compression (Fig. 8). For BGS, SEA was 1.01 J/g at  $EFPS = 2.71\%$  and 2.26 J/g at  $EFPS = 20.71\%$ . A similar trend was obtained for the SHRE topology, with a larger difference between the first two  $EFPS$  values than between the three  $EFPS$  values that were greater than 8.71%. BHS exhibited the lowest sensitivity to material ductility because the two circular arcs that formed its cell walls force controlled bending of the struts without significant plasticization before compaction of the topology at 50% compression (specimen shortening).

The results for all cases are summarized in Tables 9, 10 and 11. The SEA obtained at the lowest value of each parameter serves as the reference, and the percentage increase compared to this value is reported for each case. Table 9 compares the results for varying  $E$ . Among the topologies, the increase in SEA with  $E$  was greatest for BGS; the percentage improvement in EA capacity compared to the lowest value was ~32%. The smallest percentage increase, 14%, was observed for BHS. In Table 10, the results for the effect of  $R_e$  are collated. Increasing the yield stress significantly increased the EA efficiency of all three topologies. As yield stress increased by almost three times, SEA increased by more than two times for each topology. BGS showed the

Table 9 Comparison of the SEA values of the three topologies at different  $E$  values

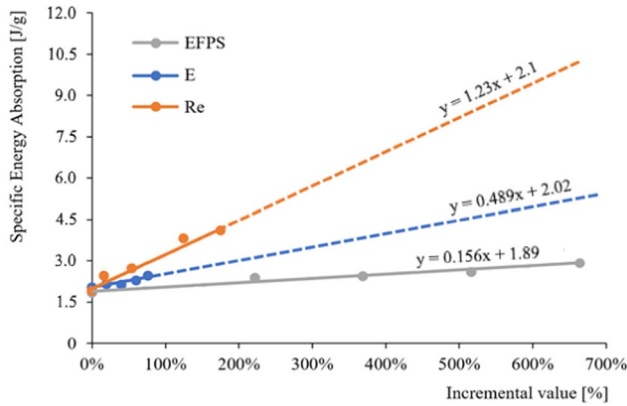
Variable parameter		BGS		BHS		SHRE	
$E$ [MPa]		SEA [J/g]		SEA [J/g]		SEA [J/g]	
1250.0	–	1.25	–	1.41	–	2.05	–
1500.0	20%	1.31	5%	1.44	2%	2.15	5%
1750.0	40%	1.53	22%	1.51	7%	2.13	4%
2000.0	60%	1.63	30%	1.57	11%	2.29	12%
2200.0	76%	1.65	32%	1.61	14%	2.46	20%

Table 10 Comparison of the SEA values of the three topologies at different  $R_e$  values

Variable parameter		BGS		BHS		SHRE	
$R_e$ [MPa]		SEA [J/g]		SEA [J/g]		SEA [J/g]	
25.8	–	1241.0	–	1.40	–	1.93	–
30.0	16%	1.42	14%	1.61	15%	2.46	28%
39.8	54%	1.77	43%	1.92	37%	2.72	41%
58.0	125%	2.36	90%	2.61	86%	3.81	98%
71.0	175%	3.18	156%	3.02	115%	4.11	114%

**Table 11** Comparison of the SEA values of the three topologies at different *EFPS* values

Variable parameter		BGS		BHS		SHRE	
<i>EFPS</i> [%]		SEA [J/g]		SEA [J/g]		SEA [J/g]	
2.71	–	1.01	–	1.20	–	1.85	–
8.71	221%	1.65	64%	1.61	32%	2.46	29%
12.71	369%	1.78	75%	1.74	45%	2.44	32%
16.71	517%	1.99	96%	1.89	58%	2.59	40%
20.71	664%	2.26	123%	1.98	65%	2.92	58%



**Fig. 14** Influence of three material parameters on the SEA of SHRE

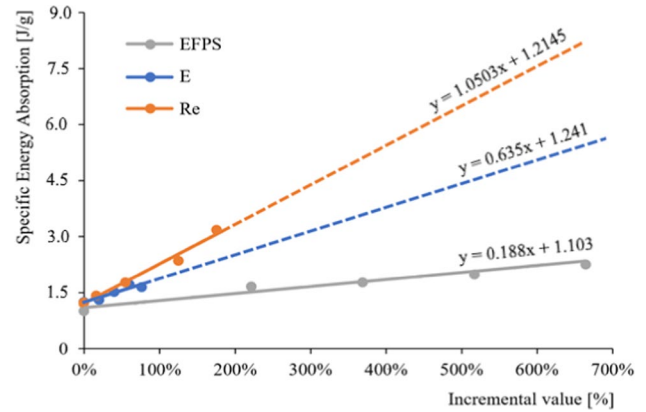


**Fig. 16** Influence of the three material properties on the SEA of BGS

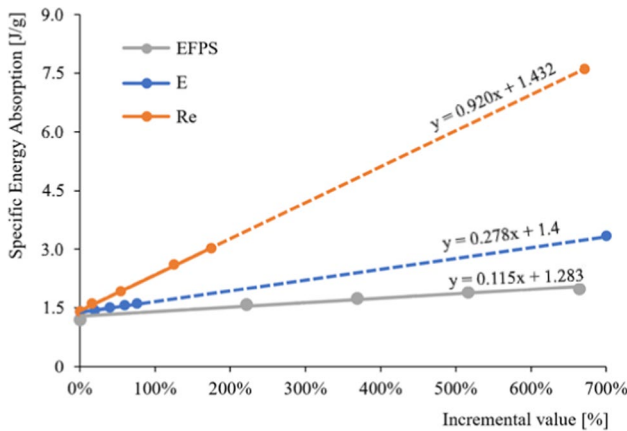


**Fig. 15** Influence of the three material parameters on the SEA of BHS

largest increase in SEA and absorbed 156% more energy at  $R_e = 71.0$  MPa than at  $R_e = 25.8$  MPa. BHS and SHRE exhibited similar changes in SEA with increasing  $R_e$ , with a maximum increase in SEA of approximately 115% compared to the reference cases. Finally, Table 11 compares the results for different values of *EFPS*. Among the topologies, this parameter had the greatest impact on BGS, with a

difference in SEA. On the contrary, the difference was only 58% for SHRE.

To demonstrate which parameter had the greatest influence on the EA of each topology representing a different main deformation mechanism, Figs. 14, 15 and 16 present SEA as a function of the percentage increase in the value of each parameter for SHRE, BHS, and BGS, respectively. Since *E* and  $R_e$  were examined within the ranges of 0%–76% and 0%–176%, respectively, the results are extrapolated to the maximum percentage increase in *EFPS*, as shown by the dashed lines in the figures. A larger slope indicates a more pronounced impact of the parameter.

Regardless of the deformation mechanism, increasing the yield stress increased the EA capacities of the cellular topologies. The highest slope was obtained for SHRE (global mechanism). The impact of yield stress on SEA was slightly smaller for BGS (plastic joint mechanism) and was lower for BHS (bending ligaments mechanism).

The impact of increasing the modulus of elasticity on SEA was greatest for BGS, slightly smaller for SHRE, and lowest for BHS. Therefore, surprisingly, when brittle failure of the material occurs, increasing the stiffness of the material is recommended. Furthermore, when global deformation with ligament buckling occurs, a higher *E* can produce better results. In the case of the plastic joint mechanism, changing

the stiffness of the material had no significant effect on the effectiveness of the EA.

Among the parameters, the *EFPS* value of the ABSplus material had the smallest impact on SEA for all topologies tested, with significantly smaller slopes than for the other two parameters. *EFPS* had the greatest effect on BGS due to brittle failure, followed by SHRE and BHS.

## 4 Summary and conclusions

In this study, the in-plane EA capacity of 2D cellular topologies under quasi-static compression loading was investigated using numerical simulations. Twenty topologies grouped into four categories, i.e., honeycomb, re-entrant, bioinspired and chiral, were tested. The influence of the basic material properties and geometric shape of ABSplus on the EA parameters was studied. The proposed topologies had the same outer dimensions and relative densities. The following conclusions can be drawn:

- The methodology presented in this paper can be used to conduct preliminary tests to identify the best prospective designs for further research. Compared to experimental tests, FEM can test numerous topology variants in a much shorter period of time. The simulation approach is also environmentally friendly, as no material is wasted to produce specimens. For research on cellular structures, appropriate constitutive models that consider phenomena inside the structure are needed. Therefore, further development and research of models is essential for accurate predictions from numerical studies. The authors are awarded that the presented methodology does not consider imperfection caused by manufacturing real specimens, e.g., imperfections and porosity, but it was not a main purpose of this study.
- Among the three main deformation mechanisms, the average EA was highest for the *plastic joint* mechanism. In most cases, the topologies exhibited high stiffness and maximum force values and the deformation process was less stable for the *bending ligaments* and *global* deformation mechanisms. In future studies, a topology with characteristic features from the tested structures will be designed to explore potential increases in the EA capacity.
- The parametric study of the material properties indicated that the yield strength had the greatest influence on SEA, regardless of the deformation mechanism. However, further studies of multiple topologies with similar deformation mechanisms are needed to support this finding.

The results of this study will be used in future research to modify the properties of cellular structures fabricated from steel material using AM technology. Furthermore, since only one value of relative density (0.3) was considered in the study, it is also planned to analyze the changes in the deformation modes for different wall thicknesses and relative densities. Analyses of the material considering porosity and voids supported by two-stage modeling at the micro- and macroscales will also be considered. In addition, dynamic blast and ballistic tests will be combined with optimization procedures to find the most efficient geometric features for very extreme loading conditions.

**Acknowledgements** The research was supported by the European Defense Agency under Grant No. B-PRJ-RT-797 and by the Interdisciplinary Center for Mathematical and Computational Modeling (ICM), University of Warsaw, under Grant No. GBE84-20.

**Author contributions** MM: conceptualization, methodology, writing—original draft, investigation, PB: conceptualization, methodology, writing—review and editing, validation, JM: supervision, funding acquisition, writing—review and editing.

**Funding** The research was supported by the European Defense Agency under Grant No. B-PRJ-RT-797 and by the Interdisciplinary Center for Mathematical and Computational Modeling (ICM), University of Warsaw, under Grant No. GBE84-20.

**Data availability** The datasets used and/or analyzed during the current study available from the corresponding author on reasonable request.

## Declarations

**Conflict of interest** The authors have no conflicts of interest to declare. All the co-authors have seen and agree with the contents of the manuscript and there is no financial interest. We certify that the submission is original and is not under review at any other publication.

**Ethical approval** Ethics approval was not required for this study.

**Open Access** This article is licensed under a Creative Commons Attribution 4.0 International License, which permits use, sharing, adaptation, distribution and reproduction in any medium or format, as long as you give appropriate credit to the original author(s) and the source, provide a link to the Creative Commons licence, and indicate if changes were made. The images or other third party material in this article are included in the article's Creative Commons licence, unless indicated otherwise in a credit line to the material. If material is not included in the article's Creative Commons licence and your intended use is not permitted by statutory regulation or exceeds the permitted use, you will need to obtain permission directly from the copyright holder. To view a copy of this licence, visit <http://creativecommons.org/licenses/by/4.0/>.

## References

1. Qi C, Remennikov A, Pei LZ, Yang S, Yu ZH, Ngo TD. Impact and close-in blast response of auxetic honeycomb-cored sandwich panels: experimental tests and numerical simulations. *Compos*

- Struct. 2017;180:161–78. <https://doi.org/10.1016/j.compstruct.2017.08.020>.
2. Xu T, Liu N, Yu Z, Xu T, Zou M. Crashworthiness design for bionic bumper structures inspired by cattail and bamboo. *Appl Bionics Biomech*. 2017. <https://doi.org/10.1155/2017/5894938>.
  3. Jackowski J, Żmuda M, Wieczorek M. Comparative analysis of small size non-pneumatic tires and pneumatic tires—radial stiffness and hysteresis, selected parameters of the contact patch. *Mainten Reliab* 2023;25:2023. <https://doi.org/10.17531/EIN/167362>.
  4. Kaczynski P, Ptak M, Wilhelm J, Fernandes FAO, de Sousa RJA. High-energy impact testing of agglomerated cork at extremely low and high temperatures. *Int J Impact Eng*. 2019;126:109–16. <https://doi.org/10.1016/j.ijimpeng.2018.12.001>.
  5. Kurzynowski T, Pawlak A, Smolina I. The potential of SLM technology for processing magnesium alloys in aerospace industry. *Arch Civ Mech Eng*. 2020;20:1–13. <https://doi.org/10.1007/S43452-020-00033-1/TABLES/3>.
  6. Leary M, Mazur M, Williams H, Yang E, Alghamdi A, Lozanovski B, et al. Inconel 625 lattice structures manufactured by selective laser melting (SLM): mechanical properties, deformation and failure modes. *Mater Des*. 2018;157:179–99. <https://doi.org/10.1016/j.matdes.2018.06.010>.
  7. Bai L, Zhang J, Chen X, Yi C, Chen R, Zhang Z. Configuration optimization design of Ti6Al4V lattice structure formed by SLM. *Materials* 2018. <https://doi.org/10.3390/ma11101856>.
  8. Rad MS, Hatami H, Ahmad Z, Yasuri AK. Analytical solution and finite element approach to the dense re-entrant unit cells of auxetic structures. *Acta Mech*. 2019;230:2171–85. <https://doi.org/10.1007/s00707-019-02387-x>.
  9. Kladovasilakis N, Tsongas K, Tzetzis D. Mechanical and feasibility characterization of fused filament fabricated triply periodic minimal surface structures. *J Compos Sci* 2021;5. <https://doi.org/10.3390/jcs5020058>.
  10. Peng C, Fox K, Qian M, Nguyen-Xuan H, Tran P. 3D printed sandwich beams with bioinspired cores: mechanical performance and modelling. *Thin-Walled Struct*. 2021;161: 107471. <https://doi.org/10.1016/j.tws.2021.107471>.
  11. L. J. Gibson, M. F. Ashby GSSinni. The mechanics of two-dimensional cellular materials. *Proc Roy Soc Lond Ser A* 1982;382.
  12. Li Z, Yang Q, Chen W, Hao H, Fang R, Cui J. Dynamic compressive properties of reinforced and kirigami modified honeycomb in three axial directions. *Thin-Walled Struct* 2022;171. <https://doi.org/10.1016/j.tws.2021.108692>.
  13. Tiwari G, Thomas T, Khandelwal RP. Influence of reinforcement in the honeycomb structures under axial compressive load. *Thin-Walled Struct*. 2018;126:238–45. <https://doi.org/10.1016/j.tws.2017.06.010>.
  14. Zhao L, Zheng Q, Fan H, Jin F. Hierarchical composite honeycombs. *Mater Des*. 2012;40:124–9. <https://doi.org/10.1016/j.matdes.2012.03.009>.
  15. Wu Y, Sun L, Yang P, Fang J, Li W. Energy absorption of additively manufactured functionally bi-graded thickness honeycombs subjected to axial loads. *Thin-Walled Struct*. 2021;164: 107810. <https://doi.org/10.1016/j.tws.2021.107810>.
  16. Dhari RS, Javanbakht Z, Hall W. On the inclined static loading of honeycomb re-entrant auxetics. *Compos Struct*. 2021;273: 114289. <https://doi.org/10.1016/j.compstruct.2021.114289>.
  17. Ingrole A, Hao A, Liang R. Design and modeling of auxetic and hybrid honeycomb structures for in-plane property enhancement. *Mater Des*. 2017;117:72–83. <https://doi.org/10.1016/j.matdes.2016.12.067>.
  18. Wu Y, Liu Q, Fu J, Li Q, Hui D. Dynamic crash responses of bio-inspired aluminum honeycomb sandwich structures with CFRP panels. *Compos B Eng*. 2017;121:122–33. <https://doi.org/10.1016/j.compositesb.2017.03.030>.
  19. Ha NS, Lu G, Xiang X. High energy absorption efficiency of thin-walled conical corrugation tubes mimicking coconut tree configuration. *Int J Mech Sci*. 2018;148:409–21. <https://doi.org/10.1016/j.ijmecsci.2018.08.041>.
  20. Yang X, Ma J, Shi Y, Sun Y, Yang J. Crashworthiness investigation of the bio-inspired bi-directionally corrugated core sandwich panel under quasi-static crushing load. *Mater Des*. 2017;135:275–90. <https://doi.org/10.1016/j.matdes.2017.09.040>.
  21. Tan C, Zou J, Li S, Jamshidi P, Abena A, Forsey A, et al. Additive manufacturing of bio-inspired multi-scale hierarchically strengthened lattice structures. *Int J Mach Tools Manuf*. 2021;167: 103764. <https://doi.org/10.1016/j.ijmachtools.2021.103764>.
  22. Li Q, Wu L, Hu L, Li E, Zou T, Liu X. Parametric analysis on axial compression performance of bio-inspired porous lattice structures. *Thin-Walled Struct*. 2023;182: 110223. <https://doi.org/10.1016/j.tws.2022.110223>.
  23. Zhang W, Yin S, Yu TX, Xu J. Crushing resistance and energy absorption of pomelo peel inspired hierarchical honeycomb. *Int J Impact Eng*. 2019;125:163–72. <https://doi.org/10.1016/j.ijimpeng.2018.11.014>.
  24. Alderson A, Alderson KL, Attard D, Evans KE, Gatt R, Grima JN, et al. Elastic constants of 3-, 4- and 6-connected chiral and anti-chiral honeycombs subject to uniaxial in-plane loading. *Compos Sci Technol*. 2010;70:1042–8. <https://doi.org/10.1016/j.compscitech.2009.07.009>.
  25. Wu W, Tao Y, Xia Y, Chen J, Lei H, Sun L, et al. Mechanical properties of hierarchical anti-tetrachiral metastructures. *Extreme Mech Lett*. 2017;16:18–32. <https://doi.org/10.1016/j.eml.2017.08.004>.
  26. Hu LL, Wu ZJ, Fu MH. Mechanical behavior of anti-trichiral honeycombs under lateral crushing. *Int J Mech Sci*. 2018;140:537–46. <https://doi.org/10.1016/j.ijmecsci.2018.03.039>.
  27. Baranowski P, Piatek P, Antolak-Dudka A, Sarzyński M, Kuciewicz M, Durejko T, et al. Deformation of honeycomb cellular structures manufactured with Laser Engineered Net Shaping (LENS) technology under quasi-static loading: experimental testing and simulation. *Addit Manuf*. 2019;25:307–16. <https://doi.org/10.1016/j.addma.2018.11.018>.
  28. Konarzewski M, Kuciewicz M, Baranowski P, Stankiewicz M, Konarzewski M, Piatek P, et al. Modelling and testing of 3D printed cellular structures under quasi-static and dynamic conditions. *Thin-Walled Struct*. 2019;145. <https://doi.org/10.1016/j.tws.2019.106385>.
  29. Kuciewicz M, Baranowski P, Małachowski J. A method of failure modeling for 3D printed cellular structures. *Mater Des* 2019;174. <https://doi.org/10.1016/j.matdes.2019.107802>.
  30. Liu Y, Zhang XC. The influence of cell micro-topology on the in-plane dynamic crushing of honeycombs. *Int J Impact Eng*. 2009;36:98–109. <https://doi.org/10.1016/j.ijimpeng.2008.03.001>.
  31. Han J, Chen H, Xu X, Li Z, Chen Q, Gu H, et al. Mechanical characterization of a novel gradient thinning triangular honeycomb. *Thin-Walled Struct*. 2023;188: 110862. <https://doi.org/10.1016/j.tws.2023.110862>.
  32. Hamzehei R, Kadkhodapour J, Anaraki AP, Rezaei S, Dariushi S, Rezaoust AM. Octagonal auxetic metamaterials with hyperelastic properties for large compressive deformation. *Int J Mech Sci*. 2018;145:96–105. <https://doi.org/10.1016/j.ijmecsci.2018.06.040>.
  33. Hedayati R, Sadighi M, Mohammadi-Aghdam M, Zadpoor AA. Mechanical properties of additively manufactured octagonal honeycombs. *Mater Sci Eng C*. 2016;69:1307–17. <https://doi.org/10.1016/j.msec.2016.08.020>.
  34. Thomas T, Tiwari G. Energy absorption and in-plane crushing behavior of aluminium reinforced honeycomb. *Vacuum*. 2019;166:364–9. <https://doi.org/10.1016/j.vacuum.2018.10.057>.
  35. Zhang D, Fei Q, Liu J, Jiang D, Li Y. Crushing of vertex-based hierarchical honeycombs with triangular substructures.

- Thin-Walled Struct. 2020;146: 106436. <https://doi.org/10.1016/j.tws.2019.106436>.
36. Qiu XM, Zhang J, Yu TX. Collapse of periodic planar lattices under uniaxial compression, part I: quasi-static strength predicted by limit analysis. *Int J Impact Eng.* 2009;36:1223–30. <https://doi.org/10.1016/j.ijimpeng.2009.05.011>.
  37. Kalubadanage D, Remennikov A, Ngo T, Qi C. Close-in blast resistance of large-scale auxetic re-entrant honeycomb sandwich panels. *J Sandwich Struct Mater.* 2021;23:4016–53. <https://doi.org/10.1177/1099636220975450>.
  38. Choudhry NK, Panda B, Kumar S. In-plane energy absorption characteristics of a modified re-entrant auxetic structure fabricated via 3D printing. *Compos B Eng.* 2022;228: 109437. <https://doi.org/10.1016/j.compositesb.2021.109437>.
  39. Xiong J, Gu D, Chen H, Dai D, Shi Q. Structural optimization of re-entrant negative Poisson's ratio structure fabricated by selective laser melting. *Mater Des.* 2017;120:307–16. <https://doi.org/10.1016/j.matdes.2017.02.022>.
  40. Günaydin K, Rea C, Kazancı Z. Energy absorption enhancement of additively manufactured hexagonal and re-entrant (auxetic) lattice structures by using multi-material reinforcements. *Addit Manuf.* 2022;59: 103076. <https://doi.org/10.1016/j.addma.2022.103076>.
  41. Wang H, Lu Z, Yang Z, Li X. A novel re-entrant auxetic honeycomb with enhanced in-plane impact resistance. *Compos Struct.* 2019;208:758–70. <https://doi.org/10.1016/j.compstruct.2018.10.024>.
  42. Wei L, Zhao X, Yu Q, Zhu G. Quasi-static axial compressive properties and energy absorption of star-triangular auxetic honeycomb. *Compos Struct.* 2021;267: 113850. <https://doi.org/10.1016/j.compstruct.2021.113850>.
  43. An MR, Wang L, Liu HT, Ren FG. In-plane crushing response of a novel bidirectional re-entrant honeycomb with two plateau stress regions. *Thin-Walled Struct.* 2022;170: 108530. <https://doi.org/10.1016/j.tws.2021.108530>.
  44. Fang J, Sun G, Qiu N, Pang T, Li S, Li Q. On hierarchical honeycombs under out-of-plane crushing. *Int J Solids Struct.* 2018;135:1–13. <https://doi.org/10.1016/j.ijsolstr.2017.08.013>.
  45. Chen Q, Pugno NM. In-plane elastic properties of hierarchical nano-honeycombs: the role of the surface effect. *Eur J Mech A/Solids.* 2013;37:248–55. <https://doi.org/10.1016/j.euromechsol.2012.06.003>.
  46. Fernandes MC, Aizenberg J, Weaver JC, Bertoldi K. Mechanically robust lattices inspired by deep-sea glass sponges. *Nat Mater.* 2021;20:237–41. <https://doi.org/10.1038/s41563-020-0798-1>.
  47. Wang P, Yang F, Fan H, Lu G. Bio-inspired multi-cell tubular structures approaching ideal energy absorption performance. *Mater Des.* 2023;225: 111495. <https://doi.org/10.1016/j.matdes.2022.111495>.
  48. Li Y, Hu D, Yang Z. Crashworthiness design of a sponge-inspired multicell tube under axial crushing. *Int J Mech Sci.* 2023;244: 108070. <https://doi.org/10.1016/j.ijmecsci.2022.108070>.
  49. Hu D, Wang Y, Song B, Dang L, Zhang Z. Energy-absorption characteristics of a bionic honeycomb tubular nested structure inspired by bamboo under axial crushing. *Compos B Eng.* 2019;162:21–32. <https://doi.org/10.1016/j.compositesb.2018.10.095>.
  50. Chen BC, Zou M, Liu GM, Song JF, Wang HX. Experimental study on energy absorption of bionic tubes inspired by bamboo structures under axial crushing. *Int J Impact Eng.* 2018;115:48–57. <https://doi.org/10.1016/j.ijimpeng.2018.01.005>.
  51. He Q, Feng J, Chen Y, Zhou H. Mechanical properties of spider-web hierarchical honeycombs subjected to out-of-plane impact loading. *J Sandwich Struct Mater.* 2020;22:771–96. <https://doi.org/10.1177/1099636218772295>.
  52. Lorato A, Innocenti P, Scarpa F, Alderson A, Alderson KL, Zied KM, et al. The transverse elastic properties of chiral honeycombs. *Compos Sci Technol.* 2010;70:1057–63. <https://doi.org/10.1016/j.compscitech.2009.07.008>.
  53. Gao D, Wang S, Zhang M, Zhang C. Experimental and numerical investigation on in-plane impact behaviour of chiral auxetic structure. *Compos Struct.* 2021;267: 113922. <https://doi.org/10.1016/j.compstruct.2021.113922>.
  54. Hu LL, Luo ZR, Zhang ZY, Lian MK, Huang LS. Mechanical property of re-entrant anti-trichiral honeycombs under large deformation. *Compos Part B Eng.* 2019;163:107–20. <https://doi.org/10.1016/j.compositesb.2018.11.010>.
  55. Qi C, Jiang F, Yu C, Yang S. In-plane crushing response of tetra-chiral honeycombs. *Int J Impact Eng.* 2019;130:247–65. <https://doi.org/10.1016/j.ijimpeng.2019.04.019>.
  56. Johnston R, Kazancı Z. Analysis of additively manufactured (3D printed) dual-material auxetic structures under compression. *Addit Manuf.* 2021;38: 101783. <https://doi.org/10.1016/j.addma.2020.101783>.
  57. Hallquist J. LS-DYNA® theory manual. 2006.

**Publisher's Note** Springer Nature remains neutral with regard to jurisdictional claims in published maps and institutional affiliations.